Applied Materials Today 21 (2020) 100826

Contents lists available at ScienceDirect

Applied Materials Today

journal homepage: www.elsevier.com/locate/apmt

Spinel-olivine microwave dielectric ceramics with low sintering temperature and high quality factor for 5 GHz wi-fi antennas

Huaicheng Xiang[a,b,c], Joni Kilpijärvi[c], Sami Myllymäki[c], Haitao Yang[b], Liang Fang[a,*], Heli Jantunen[c,*]

[a] Guangxi Key Laboratory of Optical and Electronic Materials and Devices, College of Materials Science and Engineering, Guilin University of Technology, Guilin 541004, P. R. China

[b] Shenzhen Key Laboratory of Special Functional Materials, Shenzhen Engineering Laboratory for Advanced Technology of Ceramics, Guangdong Research Center for Interfacial Engineering of Functional Materials, College of Materials Science and Engineering, College of Physics and Optoelectronic Engineering, Shenzhen University, Shenzhen 518060, P. R. China

[c] Microelectronics Research Unit, Faculty of Information Technology and Electrical Engineering, University of Oulu, FI-90014 Oulu, Finland

ARTICLE INFO

Article history:
Received 29 July 2020
Revised 2 September 2020
Accepted 5 September 2020

Keywords:
Spinel-olivine ceramics
Microwave dielectric properties
5 ghz patch antenna
Low-temperature cofiring

ABSTRACT

The patch antenna of spinel-olivine composite ceramic ($Li_2ZnGe_3O_8$-Li_2ZnGeO_4) is designed, which can realize power ratio (59%) and S_{11} of -14 dB at 5.7 GHz. The low sintering temperature (< 960 °C), low relative permittivity (8.15) and good microwave dielectric properties (quality factor ~ 32,500 GHz, resonant frequency temperature coefficient ~ -74.8 ppm/ °C) were obtained for spinel-olivine composite ceramic. $Li_2ZnGe_3O_8$-Li_2ZnGeO_4 composite microwave dielectric ceramics were synthesized at 900–980 °C using Li_2CO_3, ZnO and GeO_2, which can co-fire with silver electrodes without chemical reaction. These exceptional characteristics enable high-speed signal transmission application of spinel-olivine composite ceramics ($Li_2ZnGe_3O_8$-Li_2ZnGeO_4) in 5 GHz Wi-Fi antennas.

1. Introduction

Wireless communication technology as one of the fastest growing industries in the world, thus far, in which the application of microwave dielectric materials is indispensable [1-3]. Microwave dielectric ceramics have established their status in the field of wireless communication by reducing the size and cost of capacitors, filters, oscillators and antenna substrates. To save energy resources, their compatibilities with silver electrodes at low sintering temperatures (< 960 °C) have also become the focus of research [4-6]. The relative permittivity (ε_r), quality factor ($Q \times f$) and temperature coefficient of resonance (τ_f) are fundamental parameters for evaluating microwave dielectric properties [7,8]. In the early research of microwave dielectric ceramics, the miniaturization of the devices was the main task. Therefore, the ABO_3 type perovskites had been studied extensively because of their abundant crystal system types and simple oxide compositions, which were mainly high-temperature and high-permittivity, such as $CaTiO_3$ (S.T. ~ 1300 °C, ε_r ~ 170) [9], $SrTiO_3$ (S.T. ~ 1500 °C, ε_r ~ 200) [10]. However, the application of fifth generation (5 G) mobile technology and the chip development of electronic equipment put forward new requirements for microwave dielectric ceramics: low relative permittivity (low ε_r for higher signal propagation speed, $t_d = \sqrt{\varepsilon_r} l_e / c$,where t_d, l_e, and c denote signal delay time, transmission distance, and velocity of light) and low or ultralow temperature cofired ceramic (LTCC, ULTCC) technology [11-14]. In 2010, Sebastian and Fang et al. [15,16]. reported a spinel $Li_2ZnTi_3O_8$ microwave dielectric ceramic with low-medium permittivity, and its sintering temperature was lower than 1100 °C. Subsequently, a large number of new microwave dielectric materials with low-permittivity (10–22) for LTCC and ULTCC technology began to be widely reported, such as Lithium-based rock salt, vanadium-based garnet $A_3B_2V_3O_{12}$, molybdenum-based scheelite $AMoO_4$, etc. [17-24]. Recently, there have been new reports on the olivine-structured microwave dielectric ceramics A_2BO_4 (A = Ca, Mg, Zn; B = Si, Ge), which exhibited the characteristics of high temperature (1200–1600 °C) and lower permittivity (< 7) due to the introduction of [BO_4] tetrahedra [25-28]. Microwave dielectric ceramics are undergoing the development process from high to low permittivity and high to low sintering temperature.

In modern communication engineering, the application of dielectric materials in antennas has always been an area of concern for researchers. The high gain, high transmission and wide frequency band of antennas are the focus of current development

* Corresponding authors.
E-mail addresses: fanglianggl001@aliyun.com (L. Fang), Heli.Jantunen@oulu.fi (H. Jantunen).

https://doi.org/10.1016/j.apmt.2020.100826
2352-9407/

[29-33]. With the increasing number of mobile devices, the demand for Wi-Fi networks is also increasing. Wi-Fi signals are available in two different frequency bands: 2.4 GHz (2400–2484 MHz) and 5 GHz (4915–5875 MHz), the primary difference between them is speed [34-38]. The higher frequency requires a faster transmission speed, which is in line with the development of the low permittivity of microwave dielectric ceramics. From the perspective of crystal structure and ionic polarizability, microwave dielectric ceramics with olivine structure in Li_2O-ZnO-GeO_2 systems are suitable candidates for higher frequency Wi-Fi antennas, but high sintering temperature (1200 °C) limits their application in LTCC technology [11]. In the Li_2O-ZnO-GeO_2 phase diagram system (Fig. S1), low-temperature spinel $Li_2ZnGe_3O_8$ microwave dielectric ceramics have been reported with S.T. = 945 °C, ε_r = 10.5, $Q \times f$ = 47,400 GHz, τ_f = −63.9 ppm/ °C [39]. Therefore, by adjusting the proportion of Li_2O, ZnO and GeO_2, it is expected to obtain microwave dielectric ceramics with low permittivity and low sintering temperature that can be applied to 5 GHz Wi-Fi antennas. In the present work, we mix Li_2O, ZnO, and GeO_2 according to the molar ratio of 1:1:2, and use the solid-state reaction method to fabricate antenna substrate to realize the application of Wi-Fi signal in the 5 GHz–5.8 GHz frequency band. Moreover, the sintering temperature, phase composition after 4–16 h of sintering, microwave dielectric properties, and chemical compatibility with Ag electrode of the Li_2O-ZnO-$2GeO_2$ ceramics are investigated.

2. Experimental

2.1. Preparation of Li_2O-ZnO-GeO_2 dielectric ceramics

High purity (> 99%) raw materials of Li_2CO_3, ZnO and GeO_2 were mixed at a molar ratio of 1:1:2, and poured into a ceramic pot and milled in a high energy ball mill with ethanol and zirconia balls for 6 h with 150 rpm. After drying the ball-milled slurry in the oven at 80 °C for 48 h, the powder continued to be ground in an agate mortar, which was then placed in an alumina crucible and heated at 900 °C for 5 h with a rate of 5 °C/min. The purpose of this step was to synthesize the main phase of the Li_2O-ZnO-$2GeO_2$ materials. The calcined powder was milled for the second time, after which the 5wt% polyvinyl alcohol aqueous solution (PVA) was added as the binder and pressed the powder into cylinders with a height of 5 mm and a diameter of 10 mm. The Li_2O-ZnO-$2GeO_2$ green samples were heated to 500 °C for 10 h with a rate of 1 °C/min to remove the PVA binder. The Li_2O-ZnO-$2GeO_2$ samples were then sintered at 800–980 °C for 4 h for the measurement of dielectric properties. Further, 20wt% Ag powder was added to the sintered Li_2O-ZnO-$2GeO_2$ powder to be cofired at 940 °C for 4 h to test their chemical compatibility. The sintering temperatures of the samples were determined according to the TGA/DSC curves of the Li_2CO_3, ZnO and $2GeO_2$ powders (Fig. S2).

2.2. Fabrication of Li_2O-ZnO-$2GeO_2$ antenna substrate

The ball-milled Li_2O-ZnO-$2GeO_2$ powder was pressed into a disk-shaped green sample with a diameter of 40 mm and a thickness of 1 mm, and the green sample was sintered at 960 °C for 4 h with a rate of 5 °C min^{-1}. Both sides of the sintered sample were polished with P2000 abrasive paper (Eco-Wet, KWH Mirka Ltd., Jepua, Finland), and the sample with a thickness of about 0.8 mm was finally obtained. The silver paste (DT1402) was screen printed on the surface of the sample and allowed to stand in an oven at 150 °C for 10 min to cure the silver paste, after which the sample was sintered at 600 °C for 20 min. Finally, the sintered sample was shaped by an LPKF ProtoLaser U3 laser and assembled through an SMA (SubMiniature version A) connector.

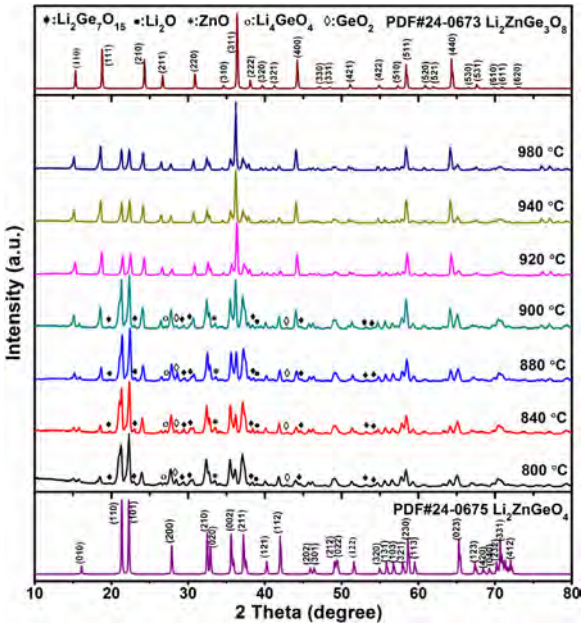

Fig. 1. XRD patterns of the Li_2O-ZnO-$2GeO_2$ ceramics sintered at 800–980 °C for 4 h.

2.3. Characterization

The phase composition and crystal structure of the Li_2O-ZnO-$2GeO_2$ ceramics were identified by X-ray powder diffraction (XRD, Bruker D8, Germany) with a Cu Kα radiation source. The microstructures were determined by field emission scanning electron microscopy (FESEM, Zeiss Ultra Plus, Germany). The Raman spectra of the sintered ceramics were measured with a Raman spectrometer (Thermo Fisher Scientific, USA). The chemical reactions between Li_2O, ZnO, and GeO_2 were evaluated by Thermogravimetric Analysis (TGA) and Differential Scanning Calorimetry (DSC, NETZSCH, Germany). The sintered ceramics were characterized with a dilatometer (DIL 402 PC/4, NETZSCH, Germany) to measure the coefficient of thermal expansion (CTE). The ε_r and $Q \times f$ were measured using the vector network analyzer (10 MHz-20 GHz, ZVB20, Rohde & Schwarz, Germany), and the τ_f values in the range of 25–85 °C were calculated by $\tau_f = \frac{f_{85}-f_{25}}{f_{25}(T_{85}-T_{25})}$ (where f_{25} and f_{85} denote resonant frequencies at 25 °C and 85 °C). The design and analysis of antenna were performed by Computer Simulation Technology (CST) and Satimo StarLab near-field antenna measurement system.

3. Results and discussion

3.1. The phase composition of Li_2O-ZnO-$2GeO_2$ ceramics

The XRD patterns of Li_2O-ZnO-$2GeO_2$ ceramics sintered at 800–980 °C for 4 h are shown in Fig. 1, where the diffraction peaks of all the samples were mainly matched well with $Li_2ZnGe_3O_8$ (PDF#24–0673) and Li_2ZnGeO_4 (PDF#24–0675). When the sintering temperature is lower than 900 °C, a small amount of impurity phase is classified, and it is also detected that the sample still contains raw materials (Li_2O, ZnO, GeO_2), indicating that the reaction at this temperature range is incomplete. When the sintering temperature is higher than 900 °C, only two phases of cubic $Li_2ZnGe_3O_8$ and orthorhombic Li_2ZnGeO_4 are detected in the sample. To determine the phase content, the two-phase Rietveld refinement was performed on the room-temperature XRD data of Li_2O-ZnO-$2GeO_2$ samples using the structures of the cubic $Li_2ZnGe_3O_8$ and orthorhombic Li_2ZnGeO_4 phase (Fig. 2a). Phase

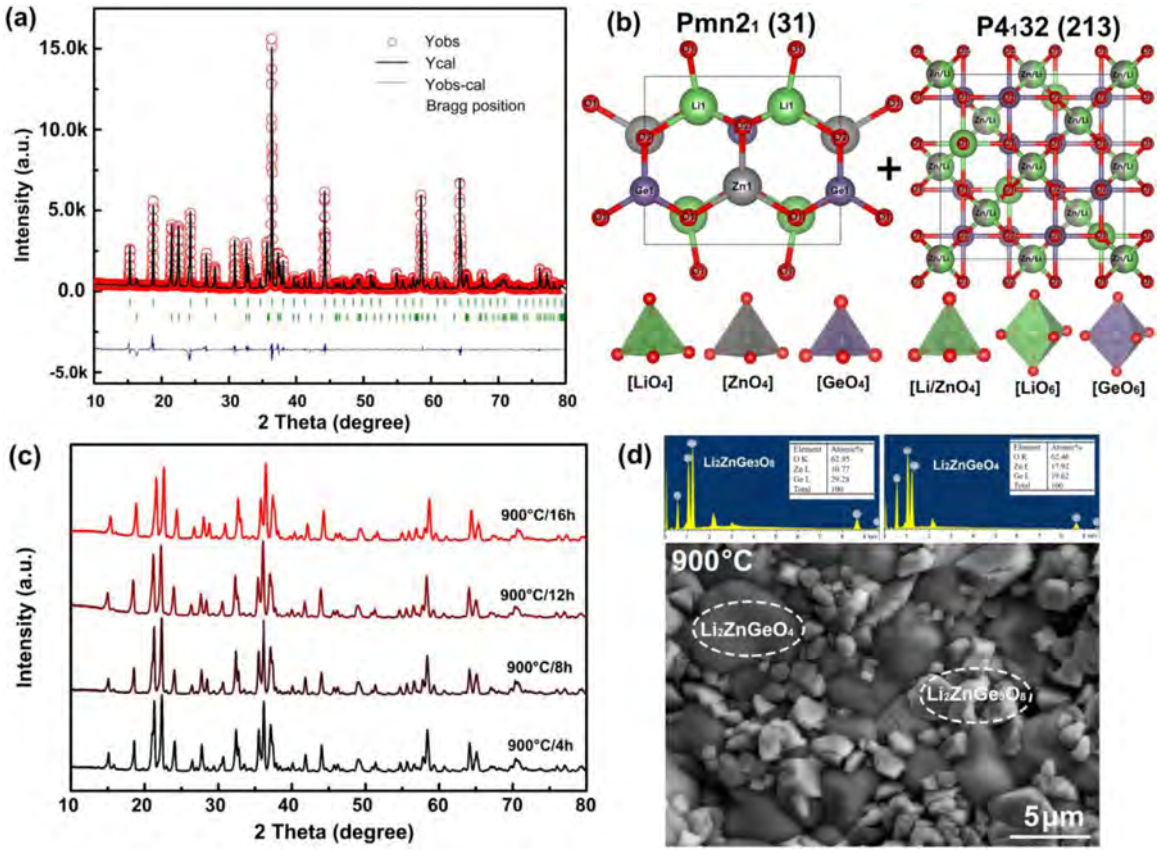

Fig. 2. (a) the Rietveld refinement pattern of Li_2O-ZnO-$2GeO_2$ ceramics sintered at 980 °C, (c) crystal structure of Li_2ZnGeO_4 and $Li_2ZnGe_3O_8$, XRD patterns of the Li_2O-ZnO-$2GeO_2$ ceramics sintered at 900 °C for 4 to 16 h, and (d) BSE image of Li_2O-ZnO-$2GeO_2$ ceramics sintered at 900 °C for 4 h.

Table 1
Phase compositions of Li_2O-ZnO-$2GeO_2$ ceramics sintered at 800–980 °C for 4 h.

S.T. (°C)	$Li_2ZnGe_3O_8$ (mol%)	Li_2ZnGeO_4 (mol%)	$Li_2Ge_7O_{15}$ (mol%)	Li_4GeO_4 (mol%)	Li_2O (mol%)	ZnO (mol%)	GeO_2 (mol%)
800	14.64	71.31	3.78	2.27	1.49	3.04	3.47
820	16.93	70.90	3.33	2.07	1.32	2.87	2.58
840	18.54	69.53	3.19	2.06	1.71	3.08	1.89
860	29.47	59.49	2.15	1.75	1.21	2.70	3.23
880	37.43	52.03	1.55	1.49	1.17	2.62	3.71
900	45.15	47.34	0.97	1.70	1.10	2.28	1.46
920	71.43	28.57	/	/	/	/	/
940	80.58	19.42	/	/	/	/	/
960	81.17	18.83	/	/	/	/	/
980	81.20	18.80	/	/	/	/	/

compositions of Li_2O-ZnO-$2GeO_2$ ceramics sintered at 800–980 °C for 4 h, as listed in Table 1. Clearly, the content of the Li_2ZnGeO_4 phase decreased with the increase of sintering temperature, while the content of $Li_2ZnGe_3O_8$ increased gradually. The maximum sintering temperature of Li_2O-ZnO-$2GeO_2$ ceramics is 980 °C, which still maintains two-phase coexistence, and neither single phase $Li_2ZnGe_3O_8$ nor new phase $Li_2ZnGe_2O_6$ can be obtained. At 800–880 °C, the orthorhombic Li_2ZnGeO_4 accounts for the leading phase and its content is 71.31–52.03%. Conversely, in the temperature range of 920–980 °C the cubic $Li_2ZnGe_3O_8$ is the dominant phase, which is more than 70%, and when the sintering temperature exceeds 940 °C, the content of $Li_2ZnGe_3O_8$ increases relatively slowly and remains above 80%. Moreover, when the sintering temperature is 900 °C $Li_2ZnGe_3O_8$ content is about 45.15%, Li_2ZnGeO_4 content is about 47.34%, and their ratio is about 1:1. In the Li_2ZnGeO_4 phase with an orthorhombic olivine structure (space group of $Pmn2_1$), the [LiO_4], [ZnO_4], and [GeO_4] tetrahedra are connected only by a corner, and all tetrahedra point to the c-axis direction. $Li_2ZnGe_3O_8$ belongs to the cubic spinel structure, in which the tetrahedral position is occupied by the random distribution of Li^+ and Zn^{2+} (8c), and the octahedral position is filled by the 1:3 ordered of Li^+ (4a) and Ge^{4+} (12d) cations (Fig. 2b).

It can be determined that when the molar ratio of Li_2O, ZnO and GeO_2 was 1:1:2, the single-phase compound $Li_2ZnGe_2O_6$ cannot be obtained after sintering at 800–980 °C for 4 h, but included the two phases $Li_2ZnGe_3O_8$ and Li_2ZnGeO_4, and the chemical reaction formula as follows:

$$2[Li_2O + ZnO + 2GeO_2] \xrightarrow{>900^\circ C} Li_2ZnGe_3O_8 + Li_2ZnGeO_4 \quad (1)$$

However, Grins et al.[40]. mixed K_2CO_3, ZnO, and GeO_2 in a molar ratio of 1:1:2, and after sintering at 752 °C for 15 h, a single-phase compound $K_2ZnGe_2O_6$ was obtained, which was similar to the $Li_2ZnGe_2O_6$ that we expected formerly. Therefore, to study whether the sintering time has a significant effect on the phase composition of Li_2O-ZnO-$2GeO_2$, the Li_2O-ZnO-$2GeO_2$ samples were sintered at 900 °C for 4 to 16 h and their XRD patterns

are shown in Fig. 2c. Obviously, with the increase of sintering time, the content changes of $Li_2ZnGe_3O_8$ and Li_2ZnGeO_4 were no obvious, which indicated that the sintering time exhibited little effect on the composition of the Li_2O-ZnO-2GeO_2, due to the substantial difference of the radius of K^+ (1.55 Å, CN = 9) and Li^+ (0.59–0.92 Å).

The electron back-scattering micrograph and energy dispersion spectra of Li2O-ZnO-2GeO2 ceramics are shown in Fig. 2d. When the Li_2O-ZnO-2GeO_2 ceramic sintered at 900 °C for 4 h, two forms of grains can be clearly observed, and their grain sizes were also quite different. According to DES analysis, the larger grain size belonged to Li_2ZnGeO_4, while the smaller grain size belonged to $Li_2ZnGe_3O_8$. Grain growth is one of the most important factors for densification in the sintering process. However, the grain sizes of the Li_2O-ZnO-2GeO_2 ceramics in low sintering temperatures (> 900 °C) are larger than those in high sintering temperatures (< 900 °C). From the perspective of two phases, the grain size of Li_2ZnGeO_4 and $Li_2ZnGe_3O_8$ increases with the increase of sintering temperature (Fig. S3). The densification of the Li_2O-ZnO-2GeO_2 ceramics was positively related to the sintering temperature. Some pores could be seen at 800 °C, and when the sintering temperature increased to 960 °C the Li_2O-ZnO-2GeO_2 sample exhibited a relatively dense microstructure with few visible pores. Fig. S4 shows the room Raman spectra of Li_2O-ZnO-2GeO_2 ceramics sintered at 800–980 °C for 4 h. Compared with Raman spectra of Li_2ZnGeO_4 and $Li_2ZnGe_3O_8$, it can be observed that Li_2O-ZnO-2GeO_2 ceramics contained these two vibration modes. According to group theory, the Raman active modes of $Li_2ZnGe_3O_8$ and Li_2ZnGeO_4 are as follows:

$$\Gamma_{(Li2ZnGe3O8)} = 7A_{1g} + 16E_g + 23F_{2g} \quad (2)$$

$$\Gamma_{(Li2ZnGeO4)} = 13A_{1g} + 10A_{2g} + 9B_{1g} + 13B_{2g} \quad (3)$$

Since Raman spectroscopy is very sensitive to changes in phase composition, it can be seen from Fig. S4 that the Raman spectra of Li_2O-ZnO-2GeO_2 ceramics have changed considerably with the increase of sintering temperature. With the increase of temperature, the peak intensity of $Li_2ZnGe_3O_8$ increased gradually (i.e. F_{2g}, E_g), which indicated that the content of $Li_2ZnGe_3O_8$ phase increases with increasing temperature, while the content of Li_2ZnGeO_4 decreased, and the Raman results further confirm the XRD analysis results.

3.2. Microwave dielectric properties of Li_2O-ZnO-2GeO_2 and its chemical compatibility with silver electrodes

Fig. 3 shows the variation of bulk densities and microwave dielectric properties of the Li_2O-ZnO-2GeO_2 ceramics with different sintering temperatures. In the orthorhombic phase dominated range (800–900 °C), Li_2O-ZnO-2GeO_2 ceramics have a lower bulk density, which is because Li_2ZnGeO_4 has a low theoretical density of 4.08 g/cm^3 [11]. With the increase of sintering temperature, the density of Li_2O-ZnO-2GeO_2 ceramics increased gradually (3.66–4.24 g/cm^3), which was due to the decrease of Li_2ZnGeO_4 phase and the increase of $Li_2ZnGe_3O_8$ phase with the increase of sintering temperature. The $Li_2ZnGe_3O_8$ with cubic phase exhibited a high theoretical density of 5.13 g/cm^3 [39]. Additionally, when the sintering temperature of Li_2O-ZnO-2GeO_2 ceramics exceeded 900 °C, the bulk density increased significantly, reaching the highest bulk density of 4.77 g/cm^3 (relative density of 96.7%) at 960 °C. The theoretical density of Li_2O-ZnO-2GeO_2 ceramics can be evaluated by $\rho_{(Li2O\text{-}ZnO\text{-}2GeO2)} \approx$ (Volume fraction of Li_2ZnGeO_4 phase × its theoretical density) + (Volume fraction of $Li_2ZnGe_3O_8$ × its theoretical density). As seen in Fig. 3a, the theoretical density of Li_2O-ZnO-2GeO_2 ceramics increased gradually as well as the bulk density, and the difference between the measured and calculated values in the low temperature was large, while the difference reduced as the increase of sintering temperature. One of the reasons is that Li_2O-ZnO-2GeO_2 ceramics are transitioning from low-density Li_2ZnGeO_4 phase to high-density $Li_2ZnGe_3O_8$ phase with the increase of temperature. Another reason is that there are still a large number of pores inside the ceramic at low temperature, and it is difficult to achieve densification.

Generally, the dielectric properties of ceramics in the microwave band are mainly determined by phonon vibration, lattice defects, ionic polarizability, densification, and secondary phases [41-43]. Since the Li_2O-ZnO-2GeO_2 ceramic mainly contains two phases of Li_2ZnGeO_4 and $Li_2ZnGe_3O_8$, the primary consideration is the effect of phase composition on its dielectric properties. The ε_r, $Q \times f$, andτ_f of composite ceramics can be estimated by the following logarithmic, series and parallel mixing rules [44,45]:

$$lg\varepsilon = \sum_{i=1}^{n} V_i \lg \varepsilon_i \quad (4)$$

$$Q^{-1} = \sum_{i=1}^{n} V_i Q_i \quad (5)$$

$$t_f = \sum_{i=1}^{n} V_i \tau_{fi} \quad (6)$$

In the equations, $\sum_{i=1}^{n} V_i = 1$, n is the number of phases in the composite ceramics, and V_i is the volume fraction of phases. As the sintering temperature increases, both the measured and calculated values of ε_r increase. The measured ε_r gradually increased from 5.63 to 8.53 in the range of 800 to 980 °C (Fig. 3b). It is worth noting that the measured value of ε_r is about 1 less than the calculated value because the density and the ionic polarizability of the ceramics will affect the permittivity, which makes the measured ε_r tend to be smaller than the calculated value. As shown in Fig. 3c, the $Q \times f$ of Li_2O-ZnO-2GeO_2 ceramic also shows an increasing trend with the sintering temperature, and its $Q \times f$ value increased from 9160 GHz to 32,500 GHz with a measurement frequency of 13.8 GHz. The Li_2O-ZnO-2GeO_2 ceramic in the range of cubic phase exhibited higher $Q \times f$ values than that of in the range of orthorhombic phase. The theoretical $Q \times f$ value of Li_2O-ZnO-2GeO_2 ceramic can be obtained by Eq. (5). There is a large error range between the measured and the theoretical values of $Q \times f$ at the sintering temperature below 900 °C, which may be caused by the low density. When the sintering temperature is higher than 900 °C, the density of Li_2O-ZnO-2GeO_2 ceramics is relatively high, which results in a good agreement between the measured and the theoretical values. In addition, the highest $Q \times f$ of 41,000 GHz was observed when the ceramic was at the measurement temperature of −40 °C and it gradually decreased as the ceramic was further heated to 85 °C (Fig. S5), which is due to the lower phonon vibrations at sub-zero temperatures [46]. As shown in Fig. 3d, the τ_f was almost stable within the measured temperature ranges with a slightly decreasing tendency (−69 ~ −75 ppm/ °C). The resonance frequency (f) showed a downward trend with increasing temperature, and Li_2O-ZnO-2GeO_2 ceramics sintered at 960 °C displayed a τ_f of −74.8 ppm/ °C in the temperature range of −40 to 85 °C (Fig. S5). The sintered Li_2O-ZnO-2GeO_2 ceramics show linear coefficient of thermal expansion (CTE) of 10.63 ppm/ °C measured in the temperature range of 25–700 °C (Fig. S6). Based on the τ_f and CTE value, the calculated temperature coefficient of relative permittivity (τ_ε) is about 128 ppm/ °C using the equation of $\tau_f = -(\tau_\varepsilon/2+\text{CTE})$.

The application requires microwave dielectric ceramics should be compatible with metal electrodes, such as Ag, Au, Cu, and their alloys. In this work, 20 wt% Ag powder was mixed with the Li_2O-ZnO-2GeO_2 powder and co-fired at 940 °C for 4 h to investigate their chemical compatibility. Fig. 4 shows the XRD pattern and BSE image of Li_2O-ZnO-2GeO_2 ceramics with 20wt% Ag sintered

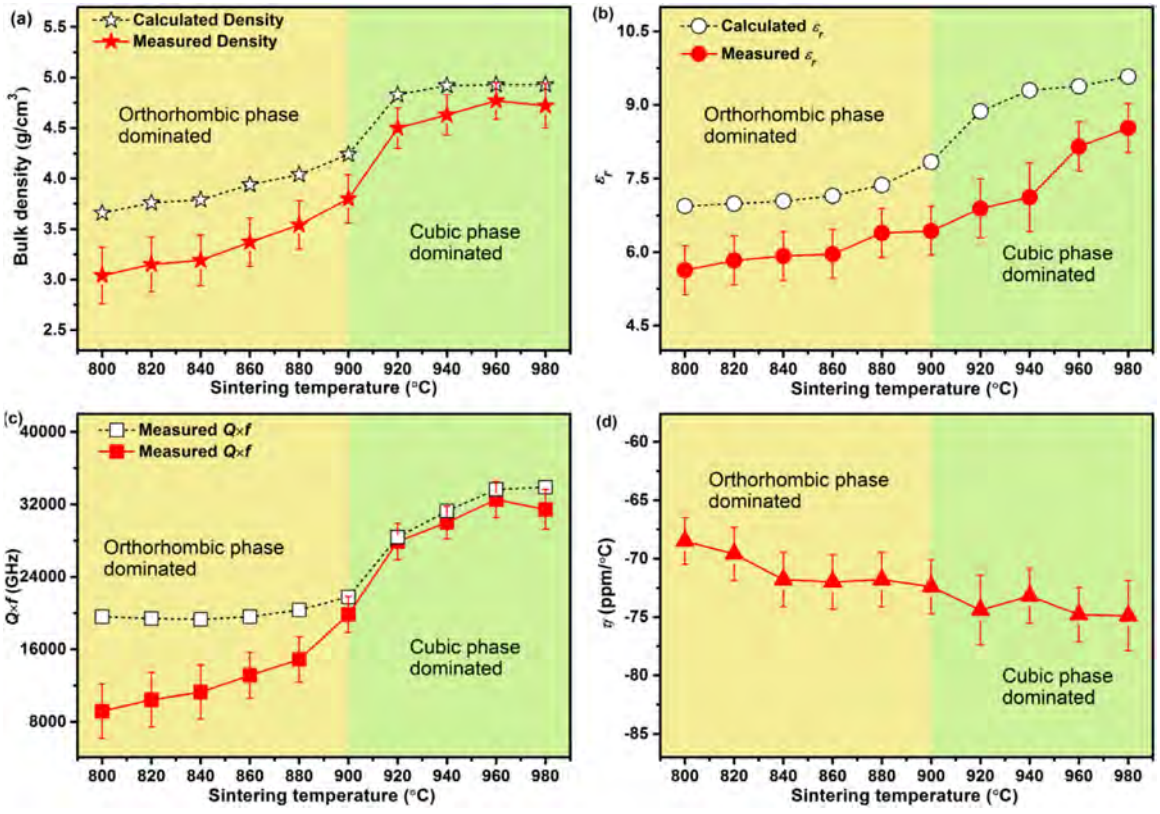

Fig. 3. Dependence of measured and calculated (a) bulk densities, (b) ε_r, (c) $Q \times f$, and (d) τ_f on sintering temperature for the Li_2O-ZnO-$2GeO_2$ ceramics.

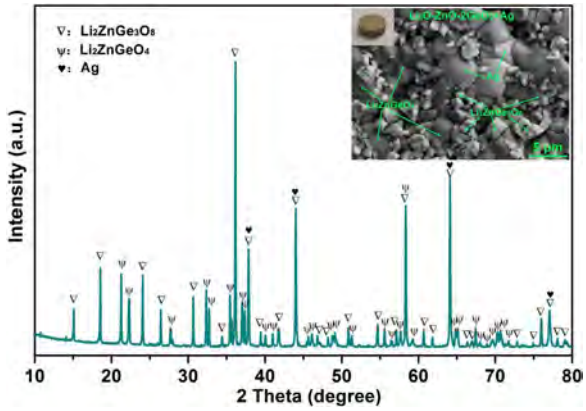

Fig. 4. XRD pattern of Li_2O-ZnO-$2GeO_2$+20wt% Ag sample sintered at 940 °C for 4 h. The inset shows the BSE image of Li_2O-ZnO-$2GeO_2$ ceramics with 20wt% Ag cofired at 940 °C.

at 940 °C for 4 h. This is further supported by the BSE image in which three distinctive types of grains were observed with clear grain boundaries. The obviously larger and brighter grains represent pure silver particles. This proves that the Li_2O-ZnO-$2GeO_2$ ceramics is fully compatible with Ag electrode.

3.3. Design of 5 GHz wi-fi antenna for Li_2O-ZnO-$2GeO_2$

We simulated and designed the Li_2O-ZnO-$2GeO_2$ antenna substrate using CST Studio Suite software. The dimensions of the square patch antenna were obtained by the following equations [47,48]:

$$W_p = \frac{c_0}{2f_r}\sqrt{\frac{2}{\varepsilon_r + 1}} \tag{7}$$

$$L_p = \frac{c_0}{2f_r\sqrt{\varepsilon_{eff}}} - 2\Delta L \tag{8}$$

where,

$$\varepsilon_{eff} = \frac{\varepsilon_r + 1}{2} + \frac{\varepsilon_r - 1}{2}\left(\frac{1}{\sqrt{1 + 12h/W_p}}\right) \tag{9}$$

in the equations, *Wp* and *Lp* are the width and length of the patch, f_r is the frequency (GHz) of the application, c_0 is the speed of light in vacuum, and ε_{eff} is the effective permittivity, and h is the thickness (mm) of the substrate.

Due to the fringe field around the patch, the patch design is slightly larger than the theoretical value to account for the difference between simulation and manufacturing. The increment to the length ΔL can be expressed as [49]:

$$\Delta L = 0.412h\frac{(\varepsilon_{eff} + 0.3)\left(\frac{W_p}{h} + 0.264\right)}{(\varepsilon_{eff} - 0.258)\left(\frac{W_p}{h} + 0.8\right)} \tag{10}$$

The calculation formulas of the width W_G and the length L_G of the Li_2O-ZnO-$2GeO_2$ antenna substrate are as follows:

$$W_G = W_p + 6h \tag{11}$$

$$L_G = L_p + 6h \tag{12}$$

A schematic diagram of the Li_2O-ZnO-$2GeO_2$ antenna substrate and its dimensions are shown in Fig. 5a. The patch length of the Li_2O-ZnO-$2GeO_2$ antenna substrate is L_p = 16.20 mm, the width W_p is 9.36 mm, and the substrate size is ($L_G \times W_G \times h$)

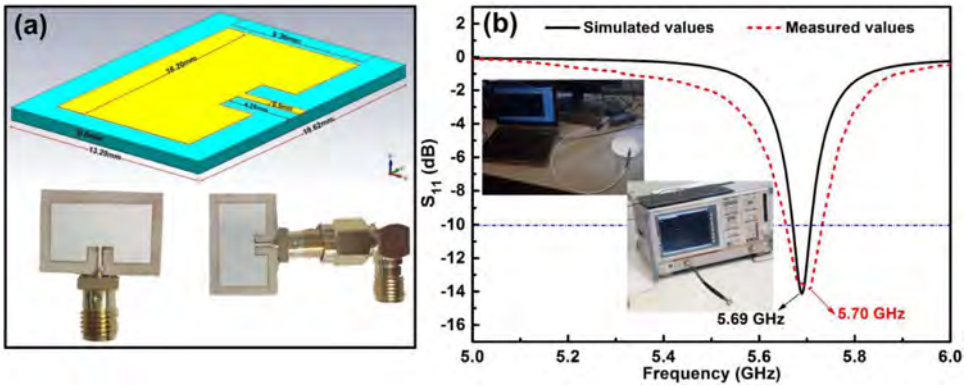

Fig. 5. (a) Patch antenna designed with CST Studio Suite software and the fabricated Li_2O-ZnO-2GeO_2 antenna. (b) Simulated and measured return loss (S_{11}).

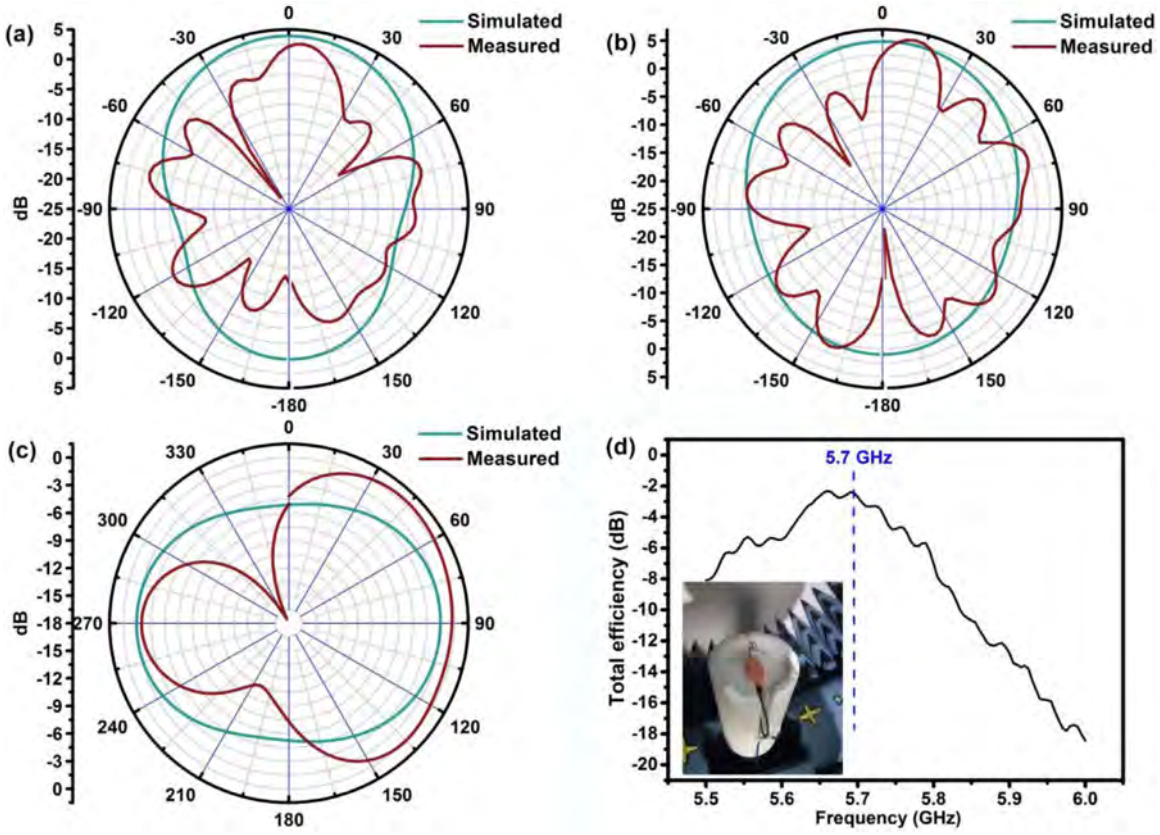

Fig. 6. The radiation patterns of the Li_2O-ZnO-2GeO_2 patch antenna at 5.7 GHz for (a) phi = 0, x-z plane, (b) phi = 90, y-z plane, (c) theta = 90, x-y plane and (d) total efficiency of the Li_2O-ZnO-2GeO_2 patch antenna at different frequencies.

19.62 mm × 13.29 mm × 0.8 mm. Fig. 5b shows the simulated and measured return loss values (S_{11}) for the Li_2O-ZnO-2GeO_2 antenna. The simulated antenna conforms to the expected properties, and the resonance frequency between the simulation result and the measurement result is in good agreement. The simulated resonance frequency is 5.69 GHz and the fabricated antenna shows 5.70 GHz. At $S_{11} = -10$ dB, the Li_2O-ZnO-2GeO_2 antenna exhibits an simulated bandwidth of 40 MHz and a measured bandwidth of 80 MHz. This difference may be due to the thickness of the patch during the manufacturing process, the ambient humidity, and the soldering of the SMA connector. Although there are differences in simulated and measured values for bandwidth, the 40–80 MHz bandwidth is still compatible with 5 GHz Wi-Fi applications.

Fig. 6 shows the measured and simulated radiation pattern at the center frequency of the 5 GHz (5–5.8 GHz) Wi-Fi band for the Li_2O-ZnO-2GeO_2 patch antenna. It can be observed that the measured and the simulated maximum antenna gain can match, but there are some differences in pattern shapes due to errors in the test environment and antenna manufacturing process. As can be seen from Fig. 6a and b, there is a similar pattern on the x-z plane (phi = 0) and the y-z plane (phi = 90) with an antenna gain of 4 dB, while antenna gain on the x-y plane (theta = 90) is the smallest. Fig. 6d shows the total efficiency of the Li_2O-ZnO-2GeO_2 patch antenna at different frequencies with a maximum of −2.3 dB at 5.7 GHz. Decibel (dB) is defined according to the power ratio:

$$dB = 10 * \log10(P_2/P_1) \quad (13)$$

where P_2 is the power being measured, and P_1 is the reference. According to Eq. (13), the Li_2O-ZnO-2GeO_2 antenna has a power ratio of 59% at 5.7 GHz. In addition to the errors of an antenna

in the manufacturing process and test environment, the antenna efficiency losses are typically due to the conduction losses, dielectric losses impedance mismatch loss [50]. Mobile phone antennas, or Wi-Fi antennas in consumer electronics products, typically have efficiencies from 20% to 70% (−7 dB −1.5 dB) [51,52]. Therefore, the spinel-olivine composite ceramics are suitable for 5 GHz Wi-Fi antenna applications.

4. Conclusion

The spinel-olivine composite ceramics were prepared at 800–980 °C by solid-state reaction. Two phases of cubic spinel $Li_2ZnGe_3O_8$ and orthorhombic olivine Li_2ZnGeO_4 were detected to coexist in the Li_2O-ZnO-2GeO_2 system, as confirmed by XRD, SEM and Raman spectroscopy. The good microwave dielectric properties (ε_r ~ 8.15, $Q \times f$ ~ 32,500 GHz, τ_f ~ −74.8 ppm/ °C) and compatible with the Ag electrode revealed that the spinel-olivine composite ceramics ($Li_2ZnGe_3O_8$-Li_2ZnGeO_4) ceramic is suitable for manufacturing 5 GHz Wi-Fi patch antenna through LTCC technology. A square patch antenna with compact dimensions of 19.62 × 13.29 × 0.8 mm was fabricated. Good agreement in terms of the radiation patterns and return loss. The measured and simulated S_{11} were obtained with the center frequency of 5.70 and 5.69 GHz and bandwidth 40 and 80 MHz, respectively. Furthermore, the spinel-olivine antenna has a power ratio of 59% at 5.7 GHz. Accordingly, the spinel-olivine antenna could be utilized for 5 GHz Wi-Fi applications.

Declaration of Competing Interest

The authors declare that they have no known competing financial interests or personal relationships that could have appeared to influence the work reported in this paper.

CRediT authorship contribution statement

Huaicheng Xiang: Conceptualization, Investigation, Methodology, Writing - original draft, Writing - review & editing. **Joni Kilpijärvi:** Methodology, Software, Writing - original draft. **Sami Myllymäki:** Methodology, Visualization, Software, Data curation. **Haitao Yang:** Methodology, Writing - review & editing. **Liang Fang:** Conceptualization, Writing - review & editing, Supervision, Funding acquisition. **Heli Jantunen:** Conceptualization, Writing - original draft, Writing - review & editing, Supervision, Funding acquisition.

Acknowledgments

The authors gratefully acknowledge the financial support from the Shenzhen Basic Research General Program (Award No. JCYJ20190808114618998), the National Natural Science Foundation of China (Award Nos. 21965009, 21761008 and 21561008) and the Natural Science Foundation of Guangxi Zhuang Autonomous Region (Award Nos. 2018GXNSFAA138175, 2018GXNSFBA281093, 2015GXNSFFA139003, and 2018GXNSFAA281093). H. Xiang and H. Jantunen acknowledge the financial support from the European Research Council Project (Award No. 24001893).

Supplementary materials

Supplementary material associated with this article can be found, in the online version, at doi:10.1016/j.apmt.2020.100826.

References

[1] M.T. Sebastian, R. Ubic, H. Jantunen, Low-loss dielectric ceramic materials and their properties, Int. Mater. Rev. 60 (2015) 392–412.
[2] N. Joseph, J. Varghese, M. Teirikangas, T. Vahera, H. Jantunen, Ultra low temperature cofired ceramic substrates with low residual carbon for the next generation microwave applications, ACS Appl. Mater. Interfaces 11 (2019) 23798–23807.
[3] D. Wang, S. Zhang, G. Wang, Y. Vardaxogloub, W. Whittowb, D. Cadmanb, D. Zhouc, K. Songa, I.M. Reaney, Cold sintered $CaTiO_3$-K_2MoO_4 microwave dielectric ceramics for integrated microstrip patch antennas, Appl. Mater. Today 18 (2020) 100519.
[4] J. Guo, X. Zhao, D.B.T. Herisson, J.H. Seo, S.S. Berbano, A.L. Baker, C. Azina, C.A. Randall, Recent progress in applications of the cold sintering process for ceramic-polymer composites, Adv. Funct. Mater. 28 (2018) 1801724.
[5] A.V. Trukhanov, V.O. Turchenko, I.A. Bobrikov, S.V. Trukhanov, I.S. Kazakevich, A.M. Balagurov, Crystal structure and magnetic properties of the $BaFe_{12-x}Al_xO19$ (x=0.1–1.2) solid solutions, J. Magn. Magn. Mater. 393 (2015) 253–259.
[6] A.L. Kozlovskiy, I.E. Kenzhina, M.V. Zdorovets, FeCo–Fe2CoO/CoO nanocomposites: Phase transformations as a result of thermal annealing and practical application in catalysis, Ceram. Int. 46 (2020) 10262–10269.
[7] D. Zhou, L.X. Pang, D.W. Wang, Z.M. Qi, I.M. Reaney, High quality factor, ultralow sintering temperature $Li_6B_4O_9$ microwave dielectric ceramics with ultralow density for antenna substrates, ACS Sustain. Chem. Eng. 6 (2018) 11138–11143.
[8] J. Li, X. Lan, X. Song, W. Lu, X. Wang, F. Shi, W. Lei, Crystal structures, dielectric properties and ferroelectricity in stuffed tridymite-type $BaAl_{(2-2x)}(Zn_{0.5}Si_{0.5})_{2x}O_4$ solid solutions, Dalton Trans 48 (2019) 3625–3634.
[9] R.C. Kell, A.C. Greenham, G.C.E. Olds, High-permittivity temperature-stable ceramic dielectrics with low microwave loss, J. Am. Ceram. Soc. 56 (1973) 352–354.
[10] C.L. Huang, S.S. Liu, Dielectric characteristics of the $(1-x)Mg_2TiO_4$–$xSrTiO_3$ ceramic system at microwave frequencies, J. Alloys Compd 471 (2009) L9–L12.
[11] C. Li, H. Xiang, M. Xu, Y. Tang, L. Fang, LiAGeO (A = Zn, Mg): two novel low-permittivity microwave dielectric ceramics with olivine structure, J. Eur. Ceram. Soc. 38 (2018) 1524–1528.
[12] H.H. Guo, D. Zhou, C. Du, P.J. Wang, W.F. Liu, L.X. Pang, Q.P. Wang, J.Z. Su, C. Singh, S. Trukhanov, Temperature stable $LiTi(Mg_{1/3}Nb_{2/3})_{0.25}O_3$-based microwave dielectric ceramics with low sintering temperature and ultra-low dielectric loss for dielectric resonator antenna applications, J. Mater. Chem. C 8 (2020) 4690–4700.
[13] S.Z. Hao, D. Zhou, F. Hussain, J.Z. Su, W.F. Liu, D.W. Wang, Q.P. Wang, Z.M. Qi, Novel scheelite-type $[Ca_{0.55}(Nd_{1-x}Bi_x)_{0.3}]MoO_4$ ($0.2\leq x\leq 0.95$) microwave dielectric ceramics with low sintering temperature, J. Am. Ceram. Soc. (2020), doi:10.1111/jace.17378.
[14] S.Z. Hao, D. Zhou, F. Hussain, W.F. Liu, J.Z. Su, D.W. Wang, Q.P. Wang, Z.M. Qi, C. Singh, S. Trukhanov, Structure, spectral analysis and microwave dielectric properties of novel $x(NaBi)_{0.5}MoO_4$-$(1-x)Bi_{2/3}MoO4$ (x=0.2-0.8) ceramics with low sintering temperatures, J. Eur. Ceram. Soc. 40 (2020) 3569–3576.
[15] S. George, M.T. Sebastian, Synthesis and microwave dielectric properties of novel temperature stable high Q, $Li_2ATi_3O_8$ (A=Mg, Zn) ceramics, J. Am. Ceram. Soc. 93 (2010) 2164–2166.
[16] H.F. Zhou, X.L. Chen, L. Fang, D.J. Chu, H. Wang, A new low-loss microwave dielectric ceramic for low temperature cofired ceramic applications, J. Mater. Res. 25 (2010) 1235–1238.
[17] D. Zhou, J. Li, L.X. Pang, D.W. Wang, I.M. Reaney, Novel water insoluble $(Na_xAg_{2-x})MoO_4$ ($0\leq x\leq 2$) microwave dielectric ceramics with spinel structure sintered at 410 degrees, J. Mater. Chem. C 5 (2017) 6086–6091.
[18] R. Gheisari, H. Chamberlain, G. Chi-Tangyie, et al., Multi-material additive manufacturing of low sintering temperature $Bi_2Mo_2O_9$ ceramics with Ag floating electrodes by selective laser burnout, Virtual Phys. Prototy. 15 (2020) 133–147.
[19] H.H. Guo, D. Zhou, W.F. Liu, L.X. Pang, D.W. Wang, J.Z. Su, Z.M. Qi, Microwave dielectric properties of temperature-stable zircon-type $(Bi,Ce)VO_4$ solid solution ceramics, J. Am. Ceram. Soc. 103 (2020) 423–431.
[20] D. Wang, S. Zhang, D. Zhou, et al., Temperature stable cold sintered $(Bi_{0.95}Li_{0.05})(V_{0.9}Mo_{0.1})O_4$-$Na_2Mo_2O_7$ microwave dielectric composites, Mater 12 (2019) 1370.
[21] L.Y. Matzui, A.V. Trukhanov, O.S. Yakovenko, L.L. Vovchenko, et al., Functional magnetic composites based on hexaferrites: correlation of the composition, magnetic and high-frequency properties, Nanomaterials 9 (2019) 1720.
[22] M.A. Darwish, A.V. Trukhanov, O.S. Senatov, et al., Investigation of AC-measurements of epoxy/ferrite composites, Nanomaterials 10 (2020) 492.
[23] L. Fang, F. Xiang, C. Su, H. Zhang, A novel low firing microwave dielectric ceramic $NaCa_2Mg_2V_3O_{12}$, Ceram. Int. 39 (2013) 9779–9783.
[24] H.C. Xiang, L. Fang, X.W. Jiang, Y. Tang, C.C. Li, A novel temperature stable microwave dielectric ceramic with garnet structure: $Sr_2NaMg_2V_3O_{12}$, J. Am. Ceram. Soc. 99 (2016) 399–401.
[25] Y. Tang, M.Y. Xu, L. Duan, J. Chen, C. Li, H. Xiang, L. Fang, Structure, microwave dielectric properties, and infrared reflectivity spectrum of olivine type Ca_2GeO_4 ceramic, J. Eur. Ceram. Soc. 39 (2019) 2354–2359.
[26] H. Xiang, C. Li, H. Jantunen, L. Fang, A.E. Hill, Ultralow loss $CaMgGeO_4$ microwave dielectric ceramic and its chemical compatibility with silver electrodes for low-temperature cofired ceramic applications, ACS Sustain. Chem. Eng. 6 (2018) 6458–6466.
[27] T. Joseph, M.T. Sebastian, Microwave dielectric properties of alkaline earth orthosilicates M_2SiO_4 (M= Ba, Sr, Ca), Mater. Lett. 65 (2011) 891–893.

[28] K.X. Song, X.M. Chen, X.C. Fan, Effects of Mg/Si ratio on microwave dielectric characteristics of forsterite ceramics, J. Am. Ceram. Soc. 90 (2007) 1808–1811.
[29] N. Joseph, J. Varghese, M. Teirikangas, H. Jantunen, A temperature responsive copper molybdate polymorph mixture near to water boiling point by a simple cryogenic quenching route, ACS Appl. Mater. Interfaces 12 (2020) 1046–1053.
[30] A.V. Trukhanov, K.A. Astapovich, M.A. Almessiere, et al., Pecularities of the magnetic structure and microwave properties in $Ba(Fe_{1-x}Scx)_{12}O_{19}$ (x<0.1) hexaferrites, J. Alloys Compd 822 (2020) 153575.
[31] D.A. Vinnik, F.V. Podgornov, N.S. Zabeivorota, et al., Effect of treatment conditions on structure and magnetodielectric properties of barium hexaferrites, J. Magn. Magn. Mater. 498 (2020) 166190.
[32] O. Yakovenko, O. Lazarenko, L. Matzui, L. Vovchenko, M. Borovoy, P. Tesel'ko, O. Lozitsky, K. Astapovich, A. Trukhanov, S. Trukhanov, Effect of Ga content on magnetic properties of $BaFe_{12-x}Ga_xO_{19}$/epoxy composites, J. Mater. Sci. 55 (2020) 9385–9395.
[33] H. Sirringhaus, N. Tessler, R.H. Friend, Integrated optoelectronic devices based on conjugated polymers, Sci 280 (1998) 1741–1744.
[34] I.J. Nam, S.M. Lee, D. Kim, Advanced monopole antenna with a wide beamwidth for the assessment of outdoor 5 G wireless communication environments, Microw. Opt. Techn. Lett. 60 (2018) 2096–2101.
[35] F.M. Schubert, M.L. Jakobsen, B.H. Fleury, Non-stationary propagation model for scattering volumes with an application to the rural LMS channel, IEEE Trans. Antennas Propag. 61 (2013) 2817–2828.
[36] K. Chandra, R.V. Prasad, B. Quang, I.G.M.M. Niemegeers, CogCell: cognitive interplay between 60 GHz picocells and 2.4/5 GHz hotspots in the 5 G era, IEEE Commun. Mag. 53 (2015) 118–125.
[37] A.V. Trukhanov, K.A. Astapovich, M.A. Almessiere, et al., Pecularities of the magnetic structure and microwave properties in $Ba(Fe_{1-x}Sc_x)_{12}O_{19}$ (x<0.1) hexaferrites, J. Alloys Compd 822 (2020) 153575.
[38] D.A. Vinnik, F.V. Podgornov, N.S. Zabeivorota, et al., Effect of treatment conditions on structure and magnetodielectric properties of barium hexaferrites, J. Magn. Magn. Mater. 498 (2020) 166190.
[39] H. Xiang, L. Fang, W. Fang, Y. Tang, C. Li, A novel low-firing microwave dielectric ceramic $Li_2ZnGe_3O_8$ with cubic spinel structure, J. Eur. Ceram. Soc. 37 (2017) 625–629.
[40] J. Grins, P.E. Werner, The crystal structure and ionic conductivity properties of $K_2ZnGe_2O_6$, Acta. Chem. Scand. 43 (1989) 11–14.
[41] C. Xing, J. Li, J. Wang, H. Chen, H. Qiao, X. Yin, Q. Wang, Z.M. Qi, F. Shi, Internal relations between crystal structures and intrinsic properties of nonstoichiometric $Ba_{1+x}MoO_4$ ceramics, Inorg. Chem. 57 (2018) 7121–7128.
[42] D. Zhou, J. Li, L.X. Pang, G.H. Chen, Z.M. Qi, D.W. Wang, I.M. Reaney, Crystal structure, infrared spectra, and microwave dielectric properties of temperature-stable zircon-type $(Y,Bi)VO_4$ solid-solution ceramics, ACS Omega 1 (2016) 963–970.
[43] M.V. Zdorovets, A.L. Kozlovskiy, The effect of lithium doping on the ferroelectric properties of LST ceramics, Ceram. Int. 46 (2020) 14548–14557.
[44] S.V. Trukhanov, I.O. Troyanchuk, N.V. Pushkarev, H. Szymczak, The influence of oxygen deficiency on the magnetic and electric properties of $La_{0.70}Ba_{0.30}MnO_3$-γ ($0 \le \gamma \le 0.30$) manganite with a perovskite structure, J. Exp. Theor. Phys. 95 (2002) 308–315.
[45] S.H. Yoon, G.K. Choi, D.W. Kim, S.Y. Cho, K.S. Hong, Mixture behavior and microwave dielectric properties of $(1-x)CaWO_4$–$xTiO_2$, J. Eur. Ceram. Soc. 27 (2007) 3087–3091.
[46] J. Varghese, T. Siponkoski, M. Sobocinski, T. Vahera, H. Jantunen, Multilayer functional tapes cofired at 450 °C: beyond HTCC and LTCC technologies, ACS Appl. Mater. Interfaces 10 (2018) 11048–11055.
[47] C.A. Balanis, Antenna theory: Analysis and Design, John wiley & sons, Inc., New York, 2016.
[48] P. Ramachandran, H. Kähäri, J. Juuti, H. Jantunen, Room temperature densified ceramics for weight optimized circular polarized GPS antenna design, Microw. Opt. Techno. Lett. 60 (2018) 1061–1066.
[49] M.H. Ullah, M.T. Islam, Design of a modified W-shaped patch antenna on Al_2O_3 ceramic material substrate for Ku-Band, Chalcogenide Lett 9 (2012) 61–66.
[50] M.H. Qaddi, M. Sonkki, S. Myllymaki, H. Mharzi, M.N. Srifi, H. Jantunen, Novel compact patch antenna for ultra-wideband (UWB) applications, Int. J. Microw. Opt. Techn. 13 (2018) 343–350.
[51] D.E. Bockelman, W.R. Eisenstadt, Combined differential and common-mode scattering parameters: theory and simulation, IEEE T. Micro. Theory 43 (1995) 1530–1539.
[52] D.C. Thompson, O. Tantot, H. Jallageas, G.E. Ponchak, M.M. Tentzeris, J. Papapolymerou, Characterization of liquid crystal polymer (LCP) material and transmission lines on LCP substrates from 30 to 110 GHz, IEEE T. Micro. Theory 52 (2004) 1343–1352.